Extended State Observer for Helicopter Mass and Center-of-Gravity Estimation

Sam Zarovy* and Mark Costello†
Georgia Institute of Technology, Atlanta, Georgia 30332

DOI: 10.2514/1.C033112

In flight estimations of helicopter mass and center of gravity are critical for health and lifecycle maintenance, flight control system feedback, and mission planning. This paper explores the use of an extended state observer for online estimation of helicopter mass and center-of-gravity location. The core algorithm is a nonlinear observer that offers provable stability properties. After describing the methodology, it is applied to a simulation of a commercial radio-controlled microcoaxial helicopter. Monte Carlo trade studies employing a comprehensive rotorcraft flight dynamics model are used to assess the algorithm's estimation accuracy in the presence of model and measurement errors. Results show the helicopter mass, longitudinal center-of-gravity location, and lateral center-of-gravity location are estimated accurately in the presence of expected errors. The vertical center-of-gravity position is more difficult to estimate due to its limited observability during typical maneuvers.

Nomenclature

A	=	rotor disk area
A_0	=	grouped angular acceleration term that does not include a rotor flap angle second derivative
C_d, C_l	=	blade element coefficients of drag and lift
C_{LR}, C_{UR}	=	coefficients of motor thrust for the lower and upper rotors
C_{lon}, C_{lat}	=	coefficients of longitudinal and lateral swashplate angles
c	=	rotor blade chord
c_X, s_X	=	cosine and sine of X
D	=	reference diameter
F_{DL}	=	body force due to vertical download
$F_{R_{XX}}$	=	total rotor forces in the XX-axis direction
$F_{RA_{XX}}$	=	aerodynamic forces in the XX-axis direction
$f_{\mathrm{CG}_{XX}}$	=	filter function for estimating vehicle center-of-gravity component XX
f_{DB}	=	deadband function
f_{DL}	=	equivalent vertical flat-plate drag area
f_m	=	filter function for estimating vehicle mass
g	=	gravity constant (9.81 $\mathrm{m/s^2}$)
H_0	=	grouped angular momentum term that does not include a rotor flap angle second derivative
$[I]$	=	moment of inertia matrix of the vehicle
$\bar{\boldsymbol{I}}_{XX}$, $\bar{\boldsymbol{J}}_{XX}$, $\bar{\boldsymbol{K}}_{XX}$	=	unit vectors in the specified XX reference frame
$\bar{\boldsymbol{I}}_{b_{XX}}$	=	moment of inertia of rotor blade in XX direction
$k_{p_{XX}}$, $k_{d_{XX}}$	=	estimation filter gains for mass and horizontal center-of-gravity location
k_{z1}, k_{z2}	=	estimation filter gains for vertical center-of-gravity location
k_β	=	rotor blade spring constant
k_1, k_2, k_3	=	extended state observer gains
L, M, N	=	components of the total external moment acting on the vehicle expressed in the body reference frame
L_B	=	distance from the rotor hinge point to the blade tip
L_{BA}, M_{BA}, N_{BA}	=	components of the fuselage aerodynamic forces expressed in the body reference frame
ℓ_1, ℓ_2, ℓ_3	=	extended state observer functions
l^*	=	distance from the rotor hinge point to the center of gravity of a rotor blade
$\mathbb{M}$	=	bound for extended state observer uncertainty error
$M_{R_{XX}}$	=	total rotor system moment about the XX axis
$M_{RA_{XX}}$	=	aerodynamic moment about the XX axis
M_S	=	spring moment about the rotor hinge point
m	=	mass of vehicle
m_b	=	mass of a rotor blade
$m_{R_{XX}}$	=	reaction moments of the rotor system acting on the airframe about the XX axis
$\tilde{m}$	=	estimate for mass of vehicle
$\mathbb{N}$	=	bound for dynamic system uncertainty derivative
N_B	=	number of rotor blades
n_m	=	number of measurements for system identification
n_p	=	number of model parameters for system identification
p, q, r	=	body reference frame components of angular rate for roll, pitch, and yaw
R_{XX}	=	reaction force of the rotor system acting on the airframe in the XX direction
$\bar{\boldsymbol{r}}_{A\to B}$	=	position vector from point A to point B
$\tilde{r}_{\mathrm{CG}_{XX}}$	=	estimate of center-of-gravity location in the XX direction
S	=	reference area
$S_X(\boldsymbol{Y})$	=	skew-symmetric matrix representation of the vector $\boldsymbol{Y}$ expressed in the reference frame X
T	=	rotor thrust
$[T_{A\to B}]$	=	transformation matrix from frame A to frame B
t	=	current time
u, v, w	=	translational velocity components of the vehicle mass center expressed in the body reference frame
u_{CP}, v_{CP}, w_{CP}	=	translational velocity components at the center of pressure expressed in the body reference frame
u_{LR}, u_{UR}	=	lower and upper motor throttle inputs

Received 24 July 2014; revision received 29 January 2015; accepted for publication 9 March 2015; published online 13 August 2015.

*Graduate Research Assistant, Guggenheim School of Aerospace Engineering; currently Modeling and Simulation Engineer, Charles Stark Draper Laboratory, Inc., Cambridge, MA 02139.

†Lewis Professor, Guggenheim School of Aerospace Engineering, Woodruff School of Mechanical Engineering.

u_R, u_T, u_P	=	aerodynamic velocity components at a rotor blade element aerodynamic center in the radial, tangential, and perpendicular directions
u_w, v_w, w_w	=	wind-velocity components expressed in the body reference frame
u_ϕ, u_θ	=	longitudinal and lateral cyclic swashplate inputs
V	=	body translational velocity magnitude
V_c	=	vertical climb velocity
V_{CP}	=	velocity magnitude at the center of pressure
$V_{\text{atm}_{XX}}$	=	atmospheric wind disturbance components expressed in the XX direction
$V_{0_{XX}}$	=	body translational velocity component expressed in the hub frame XX direction
v_h	=	induced inflow velocity at hover
v_i	=	induced inflow velocity
v_k	=	measurement value with noise
$\bar{\boldsymbol{v}}$	=	average velocity of the rotor wake
$\bar{\boldsymbol{v}}_{\text{CG}}$	=	translational velocity vector of the vehicle's center of gravity
X, Y, Z	=	components of the total external force acting on the vehicle expressed in the body reference frame
X_{BA}, Y_{BA}, Z_{BA}	=	components of the fuselage aerodynamic forces expressed in the body reference frame
X_G, Y_G, Z_G	=	components of the force due to gravity acting on the vehicle expressed in the body reference frame
x, y, z	=	position vector components of vehicle expressed in the inertial reference frame
x_1, x_2	=	dynamic system states
$\tilde{x}_1, \tilde{x}_2, \tilde{x}_3$	=	dynamic system state estimates from the extended state observer
y_k	=	state truth value
α	=	angle of attack
β	=	rotor blade flapping angle
$\beta_0, \beta_{1C}, \beta_{1S}$	=	rotor blade collective, longitudinal cyclic, and lateral cyclic flapping angles
Δ	=	model uncertainty
$\Delta D, \Delta L$	=	blade element lift and drag
Δr	=	blade element width
δ	=	saturation function boundary-layer thickness
ϵ	=	extended state observer update parameter
ε	=	rotor blade hinge offset
η_k	=	measurement noise
η_1, η_2, η_3	=	extended state observer error terms
$\bar{\boldsymbol{\eta}}$	=	extended state observer error vector
$\theta(t)$	=	rotor blade
$\theta_0, \theta_{1C}, \theta_{1S}$	=	rotor blade collective, cyclic longitudinal, and lateral pitch angles
θ_{twist}	=	rotor blade twist pitch
ρ	=	atmospheric density
τ_M	=	motor time constant
τ_{SW}	=	swashplate time constant
ϕ, θ, ψ	=	Euler rotation angles for roll, pitch, and yaw
ψ_R	=	rotor blade azimuth angle
Ω	=	angular rate of rotor in the shaft frame
$\Omega_{\text{LR}}, \Omega_{\text{UR}}$	=	angular velocity of the lower and upper rotors
$\Omega_{0_{XX}}$	=	angular velocity components of the hub frame with respect to the inertial frame
$\bar{\boldsymbol{\omega}}_{X/Y}$	=	angular velocity vector of reference frame X with respect to reference frame Y

Subscripts

B	=	body
BL	=	rotor blade
H	=	hub
I	=	inertial
S	=	shaft

I. Introduction

THE utility of rotorcraft has enabled them to fly a wide array of civilian and military missions, many of which require operations resulting in a the quick change of vehicle mass and center-of-gravity (CG) location, such as the loading or unloading of cargo and troops, the pickup and transportation of injured persons, the dropping of water to fight forest fires, etc. These missions commonly occur in dangerous environments or under time constraints when a thorough measurement of the mass properties of passengers or payload is not realistic. Uncertainty due to mass loading can affect stability, performance, maintenance costs, and fuel economy of rotorcraft. As a result, inflight estimation of vehicle mass and CG location are increasingly important for rotorcraft operations. Current flight conditions can be fed back to advanced automatic flight control systems for mission planning to ensure safe operation in various flight regimes as well as enhance gain scheduling to maintain desired vehicle handling qualities. Additionally, mass properties can be used for condition-based maintenance as part of a health-and-usage monitoring system to properly estimate the fatigue and wear of components, which reduces operating costs and improves safety.

Multiple methods have been presented for estimation of vehicle mass properties in flight. Bateman patented a method to measure the weight and center-of-gravity location through the landing gear before takeoff and then used the aircraft's fuel burn rate to estimate movement of the CG in flight [1]. Glover patented a technique that combined the measurements of two accelerometers, one placed in the front of the aircraft and one placed in the rear, to capture the pitching motion of the aircraft for longitudinal CG location estimation [2]. Moffatt used hover performance charts to develop a helicopter estimation algorithm that was a function of engine torque, altitude, pressure, and atmospheric temperature [3]. More recent methods include neural-network-based approaches such as the work of Morales and Haas, who used a neural network to estimate the helicopter gross weight in the hover regime [4]. Bi et al. employed a neural network for inflight estimation of the gross weight and CG location for the V-22 [5]. Idan et al. trained a neural network to estimate the weight and CG at various trimmed flight conditions: hover, climb, cruise, decent, etc. [6]. Overall, neural networks have been shown to adequately estimate helicopter mass properties if properly trained. However, training can be intensive and requires a sufficient amount of data. Another recent method is the extended Kalman filter (EKF) technique proposed by Abraham and Costello, which fuses sensor data and a system model for mass properties state estimation in the presence of measurement error [7]. Taylor and Rogers applied this EKF technique to experimentally estimate the weight of a radio-controlled helicopter [8]. In both efforts [7,8], an EKF was shown to accurately estimate the weight and CG location, although the accuracy degraded with increasing model and measurement errors. Apetre et al. combined a neural network with an EKF to create a hybrid algorithm that leveraged both approaches to improve estimations while combating each method's individual issues [9]. There are two main difficulties with an EKF-based mass properties estimation algorithm. Extended Kalman filters are sensitive to model errors, resulting in significant estimation errors of the mass and CG location. Furthermore, the linearization of the system for state propagation and measurement state update leads to a filter that is not necessarily stable and can diverge [10]. This is especially true for highly nonlinear plants.

In this work, an extended state observer (ESO)-based algorithm is developed for helicopter mass and CG estimation. First proposed by Han [11], the ESO is a high-gain observer with an augmented state to estimate uncertainty in the system dynamics from any unknown source of error, such as model mismatch or an external disturbance. The ESO is a critical component of active disturbance rejection control (ADRC) algorithms. Also developed by Han [12], ADRC combines the nonlinear feedback of a dynamic inversion controller with an ESO, using an estimation of model uncertainty and external disturbances to enable precise control. The ADRC architecture including an ESO has been applied in a variety of engineering fields, including tension controls for industrial web tension regulation by

Hou et al. [13], precise motion control of robotic platforms by Su et al. [14], aircraft flight control by Huang et al. [15], and rejection of vertical and yaw channel gusts for an unmanned rotorcraft by Martini et al. [16] and Lénoard et al. [17]. Since model mismatch caused by uncertainty in mass and CG location can be estimated as part of the total disturbance of a system, an ESO algorithm can be implemented to estimate helicopter mass properties in real time. A nice feature of the ESO is that it enables rigorous proof of observer stability for nonlinear systems. This is, of course, in contrast to extended Kalman filters that do not possess this feature.

This paper begins with a description of a comprehensive flight dynamics simulation of a commercial radio controlled (RC) helicopter. Then, a description of the general ESO algorithm is given, followed by details of the mass and CG estimation algorithm for the nonlinear helicopter model; after which, the results of Monte Carlo simulation trade studies for the algorithm given model and measurement error are presented, along with conclusions for this work.

II. Coaxial Helicopter Dynamic Model

A mass and CG location estimation algorithm based on an ESO is applied to a nonlinear coaxial helicopter model to assess its usefulness. The dynamic model is based on a commercial radio-controlled microcoaxial helicopter; Fig. 1. The vehicle weighs 60 g and has a main rotor diameter of 176 mm, with two blades per rotor. The rotorcraft's two counterrotating rotors are driven by electric motors. Thrust is controlled by changing the speed of each rotor simultaneously, whereas yaw control is achieved through changing the speed of each rotor differentially. The microcoaxial helicopter is also outfitted with a wireless inertial-measurement-unit (IMU) circuit board developed by the University of California, Berkeley [18]. This board acts as a sensor mote (a node in a wireless sensor network), providing telemetry as well as control of servomotors and motors. Information is transmitted to and from the vehicle using a universal serial bus (USB) base station. This section provides a development of all the major flight dynamic model components as well as the experiments performed for system identification and model validation.

The translational velocity of vehicle center of gravity can be expressed as

$$\bar{\boldsymbol{v}}_{\mathrm{CG}} = \dot{x}\bar{\boldsymbol{I}}_I + \dot{y}\bar{\boldsymbol{J}}_I + \dot{z}\bar{\boldsymbol{K}}_I = u\bar{\boldsymbol{I}}_B + v\bar{\boldsymbol{J}}_B + w\bar{\boldsymbol{K}}_B \tag{1}$$

where I and B represent the inertial and body reference frames. The inertial reference frame I is attached to the ground, assuming a flat-Earth approximation and $\bar{\boldsymbol{K}}_I$ down. The body reference frame B is fixed to the vehicle with its origin at the center of gravity. The $\bar{\boldsymbol{I}}_B$ vector points out the vehicle nose, $\bar{\boldsymbol{J}}_B$ out the right or starboard side, and $\bar{\boldsymbol{K}}_B$ down out the bottom of the vehicle. The body frame is related to the inertial frame through the conventional Euler angle transformation. Thus, the inertial and body frame velocity components are related through the translational kinematic differential equations:

$$\begin{Bmatrix} \dot{x} \\ \dot{y} \\ \dot{z} \end{Bmatrix} = \begin{bmatrix} c_\theta c_\psi & s_\phi s_\theta c_\psi - c_\phi s_\psi & c_\phi s_\theta c_\psi + s_\phi s_\psi \\ c_\theta s_\psi & s_\phi s_\theta s_\psi + c_\phi c_\psi & c_\phi s_\theta s_\psi - s_\phi c_\psi \\ -s_\theta & s_\phi c_\theta & c_\phi c_\theta \end{bmatrix} \begin{Bmatrix} u \\ v \\ w \end{Bmatrix} \tag{2}$$

where $c_X = \cos(X)$ and $s_X = \sin(X)$. The angular velocity of the vehicle with respect to the inertial frame is written as

$$\bar{\boldsymbol{\omega}}_{B/I} = \dot{\phi}\bar{\boldsymbol{I}}_B + \dot{\theta}\bar{\boldsymbol{J}}_N + \dot{\psi}\bar{\boldsymbol{K}}_I = p\bar{\boldsymbol{I}}_B + q\bar{\boldsymbol{J}}_B + r\bar{\boldsymbol{K}}_B \tag{3}$$

where N is an intermediate frame in the conventional Euler angle rotation. The rotational kinematic differential equations can be expressed as

$$\begin{Bmatrix} \dot{\phi} \\ \dot{\theta} \\ \dot{\psi} \end{Bmatrix} = \begin{bmatrix} 1 & s_\phi t_\theta & c_\phi t_\theta \\ 0 & c_\phi & -s_\phi \\ 0 & s_\phi / c_\theta & c_\phi / c_\theta \end{bmatrix} \begin{Bmatrix} p \\ q \\ r \end{Bmatrix} \tag{4}$$

The translational and rotational dynamic equations of the vehicle center of gravity are expressed in the body frame as

$$\begin{Bmatrix} \dot{u} \\ \dot{v} \\ \dot{w} \end{Bmatrix} = \begin{bmatrix} 0 & r & -q \\ -r & 0 & p \\ q & -p & 0 \end{bmatrix} \begin{Bmatrix} u \\ v \\ w \end{Bmatrix} + \begin{Bmatrix} X/m \\ Y/m \\ Z/m \end{Bmatrix} \tag{5}$$

$$\begin{Bmatrix} \dot{p} \\ \dot{q} \\ \dot{r} \end{Bmatrix} = [I]^{-1} \begin{bmatrix} 0 & r & -q \\ -r & 0 & p \\ q & -p & 0 \end{bmatrix} [I] \begin{Bmatrix} p \\ q \\ r \end{Bmatrix} + [I]^{-1} \begin{Bmatrix} L \\ M \\ N \end{Bmatrix} \tag{6}$$

where m is the vehicle mass; $[I]$ is the mass moment of inertia matrix; and X, Y, Z, L, M, and N are the summed external forces and moments acting on the vehicle. The major external forces and moments are gravity, aerodynamic drag, and download due to the rotor wake as well as the forces and moments due to the vertical tail, the rotors, and the flybar.

The major components of the nonlinear rotorcraft model include aircraft dynamics; rotor inflow and wake modeling; control motor

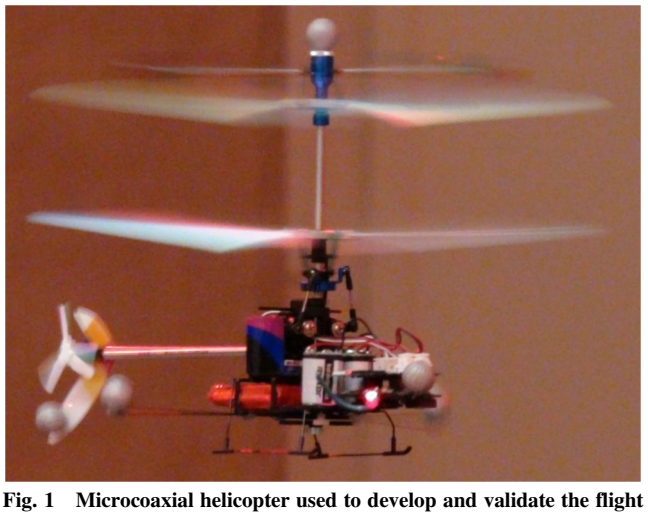

Fig. 1 Microcoaxial helicopter used to develop and validate the flight dynamics model.

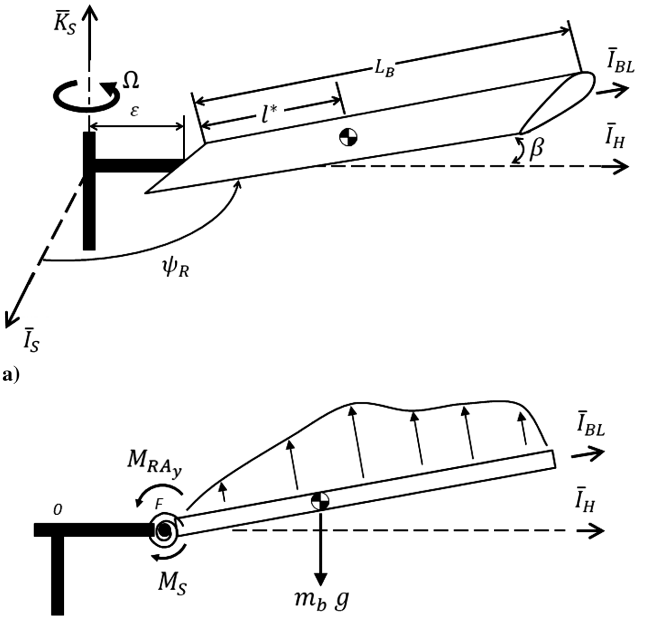

Fig. 2 Illustrations of rotor blade model: a) relevant parameters and states, and b) relevant free body diagram of blade forces and moments.

and servomotor dynamics; and a rotor system model used to simulate nonlinear rotor flapping dynamics and calculate rotor loads for the lower rotor, upper rotor, and flybar.

The rotor system model employs a blade-element-based numerical algorithm to calculate flapping dynamics and constraint loads, as illustrated in Fig. 2. The reference frames associated with rotor flapping are the shaft frame S (fixed to the nonrotating shaft with its origin at the rotor hub, $\bar{\boldsymbol{I}}_S$ pointing toward the vehicle tail, and $\bar{\boldsymbol{K}}_S$ pointing up), the hub frame H (fixed to rotating rotor hub with $\bar{\boldsymbol{I}}_H$ pointing along the rotor blade and $\bar{\boldsymbol{K}}_H$ pointing upward along the rotor shaft), and the blade frame BL (fixed to rotor blade with $\bar{\boldsymbol{I}}_{\mathrm{BL}}$ along the blade, $\bar{\boldsymbol{J}}_{\mathrm{BL}}$ pointing out the leading edge, and $\bar{\boldsymbol{K}}_{\mathrm{BL}}$ pointing up). The flexible rotor blade is approximated as rigid with an effective hinge offset and associated spring constant. Additionally, it is assumed that the rotor dynamics are sufficiently faster than the vehicle body dynamics, such that the body rates are constant in the rotor flapping dynamic equations. The individual blade flapping dynamics are derived by taking the sum of moments about the blade hinge point F, as shown in Fig. 2b. A single-degree-of-freedom equation of motion for blade flapping is formulated by solving for the second derivative of the flap angle:

$$\ddot{\beta} = \frac{M_{RA_y} + k_\beta \beta + m_b g l^* c_\beta - H_0 + m_b l^* A_0}{-I_{b_{yy}} - m_b l^{*2}} \tag{7}$$

where M_{RA_y} is the aerodynamic moment generated by the rotor about $\bar{\boldsymbol{J}}_H$; k_β is the torsional spring constant; and H_0 and A_0 represent, respectively, the grouped angular momentum and acceleration terms that do not include a second derivative of the flap angle.

The aerodynamic forces and moments generated by the rotor are calculated by splitting the rotor blade into a finite number of elements. The radial, tangential, and perpendicular aerodynamic velocity components (u_R, u_T, u_P) are a function of the hub velocity, body angular velocity, rotor angular velocity, induced rotor inflow, and wind disturbances at the blade section

$$\begin{Bmatrix} u_R \\ u_T \\ u_P \end{Bmatrix} = \begin{Bmatrix} V_{0_x} \\ V_{0_y} \\ V_{0_z} \end{Bmatrix} + \begin{bmatrix} 0 & -\Omega_{0_z} & \Omega_{0_y} \\ \Omega_{0_z} & 0 & -\Omega_{0_x} \\ -\Omega_{0_y} & \Omega_{0_x} & 0 \end{bmatrix} \begin{Bmatrix} r_{0\to F_x} \\ r_{0\to F_y} \\ r_{0\to F_z} \end{Bmatrix} + \begin{bmatrix} 0 & -\omega_{\mathrm{BL}/I_z} & \omega_{\mathrm{BL}/I_y} \\ \omega_{\mathrm{BL}/I_z} & 0 & \omega_{\mathrm{BL}_x} \\ -\omega_{\mathrm{BL}/I_y} & \omega_{\mathrm{BL}/I_x} & 0 \end{bmatrix} \begin{Bmatrix} r_{F\to p_x} \\ r_{F\to p_y} \\ r_{F\to p_z} \end{Bmatrix} - \begin{Bmatrix} v_{\mathrm{atm}_x} \\ v_{\mathrm{atm}_y} \\ v_{\mathrm{atm}_z} \end{Bmatrix} - \begin{Bmatrix} 0 \\ 0 \\ v_i \end{Bmatrix} \tag{8}$$

where $r_{0\to F_x}$, $r_{0\to F_y}$, and $r_{0\to F_z}$ are the position vector components from the hub center to the blade hinge point; $r_{F\to p_x}$, $r_{F\to p_y}$, and $r_{F\to p_z}$ are the position vector components from the blade hinge point to the center of blade element section; V_{0_x}, V_{0_y}, and V_{0_z} are the hub velocity components; V_{atm_x}, V_{atm_y}, and V_{atm_z} are the atmospheric wind disturbance components; Ω_{0_x}, Ω_{0_y}, and Ω_{0_z} are the angular velocity components of the hub frame with respect to the inertial frame; ω_{BL/I_x}, ω_{BL/I_y}, and ω_{BL/I_z} are the angular velocity components of the blade frame with respect to the inertial frame; and v_i is the induced rotor inflow velocity.

Blade pitch is controlled through the swashplate as

$$\theta(t) = \theta_0 + \theta_{\mathrm{twist}} \frac{\varepsilon + r_{F\to p_x}}{\varepsilon + L} - \theta_{1C}(t)\cos(\psi_R) - \theta_{1S}(t)\sin(\psi_R) \tag{9}$$

where θ_0 is the collective pitch, θ_{twist} is the blade twist, θ_{1C} is the longitudinal cyclic pitch, and θ_{1S} is the lateral cyclic pitch. Given the velocity components and blade pitch, the section rotor aerodynamic loads are expressed in Eqs. (10) and (11). The aerodynamic forces and moments for each element section can then be summed over the blade to obtain the total rotor blade aerodynamic load:

$$\begin{Bmatrix} \Delta F_{RA_x} \\ \Delta F_{RA_y} \\ \Delta F_{RA_z} \end{Bmatrix} = \begin{Bmatrix} 0 \\ -c_\phi \Delta D - s_\phi \Delta L \\ c_\phi \Delta L - s_\phi \Delta D \end{Bmatrix} = \frac{1}{2}\rho \mathrm{V}^2 c \Delta r \begin{Bmatrix} 0 \\ -c_\phi C_d - s_\phi C_l \\ c_\phi C_l - s_\phi C_d \end{Bmatrix} \tag{10}$$

$$\begin{Bmatrix} \Delta M_{RA_x} \\ \Delta M_{RA_y} \\ \Delta M_{RA_z} \end{Bmatrix} = \mathbb{S}_H(\bar{\boldsymbol{r}}_{F\to P}) \begin{Bmatrix} \Delta F_{RA_x} \\ \Delta F_{RA_y} \\ \Delta F_{RA_z} \end{Bmatrix} \tag{11}$$

Although the preceding equations developed are for a single blade, a rotor system with N_B blades will have N_B degrees of freedom associated with the rigid rotor blade flapping. Rather than modeling each blade individually, the entire rotor system is modeled as a whole. Since the blade pitch control inputs excite the system in a first harmonic manner, it is reasonable to assume the main flapping response is also first harmonic:

$$\beta(t) = \beta_0(t) + \beta_{1C}(t)\cos(\psi_R) + \beta_{1S}(t)\sin(\psi_R) \tag{12}$$

where β_0 is the coning angle, β_{1C} is the longitudinal flap angle, and β_{1S} is the lateral flap angle.

It should be noted that the transformation from individual blade to multiblade coordinates is general in nature and capable of representing higher fidelity than first harmonic motion; however, this approximation captures the majority of the rotor motion for flight dynamics purposes. The three equations of motion for first harmonic flapping are found through harmonic balancing [19], where the first harmonic expansion is substituted into the flapping equations of motion and the constant, cosine, and sine harmonic components are calculated:

$$\ddot{\beta}_0 = \frac{1}{2\pi}\int_0^{2\pi} \ddot{\beta}\, \mathrm{d}\psi_R \tag{13}$$

$$\ddot{\beta}_{1C} = \beta_{1C}\Omega^2 - 2\Omega\dot{\beta}_{1S} + \frac{1}{\pi}\int_0^{2\pi} \ddot{\beta}\, \cos(\psi_R)\, \mathrm{d}\psi_R \tag{14}$$

$$\ddot{\beta}_{1S} = \beta_{1S}\Omega^2 + 2\Omega\dot{\beta}_{1C} + \frac{1}{\pi}\int_0^{2\pi} \ddot{\beta}\, \sin(\psi_R)\, \mathrm{d}\psi_R \tag{15}$$

In the preceding equations, Ω is the rotor angular velocity and $\ddot{\beta}$ is calculated from Eq. (7). The rotor forces and moments transferred to the vehicle frame are the reaction forces and moments at the rotor blade effective flap hinge joint.

For flight dynamics analysis, the constant rotor loads are the primary interest, and the total rotor forces and moments on the parent vehicle body are summed over the entire rotor disk, as shown in Eqs. (16) and (17):

$$\begin{Bmatrix} F_{R_X} \\ F_{R_Y} \\ F_{R_Z} \end{Bmatrix} = \frac{N_B}{2\pi}\int_0^{2\pi} -[T_{B\to H}]^T [T_{H\to \mathrm{BL}}]^T \begin{Bmatrix} R_X \\ R_Y \\ R_Z \end{Bmatrix} \mathrm{d}\psi_R \tag{16}$$

$$\begin{Bmatrix} M_{R_X} \\ M_{R_Y} \\ M_{R_Z} \end{Bmatrix} = \frac{N_B}{2\pi}\int_0^{2\pi} -[T_{B\to H}]^T [T_{H\to \mathrm{BL}}]^T \begin{bmatrix} 1 & 0 \\ 0 & 0 \\ 0 & 1 \end{bmatrix} \begin{Bmatrix} m_{R_X} \\ m_{R_Z} \end{Bmatrix} \mathrm{d}\psi_R + \frac{N_B}{2\pi}\int_0^{2\pi} -[T_{B\to H}]^T \begin{bmatrix} 0 & 0 & 0 \\ 0 & 0 & -\varepsilon \\ 0 & \varepsilon & 0 \end{bmatrix} [T_{H\to \mathrm{BL}}]^T \begin{Bmatrix} R_X \\ R_Y \\ R_Z \end{Bmatrix} \mathrm{d}\psi_R \tag{17}$$

where R_{XX} and $m_{R_{XX}}$ are the reaction forces and moments of a rotor blade, and $[T_{B\to H}]$ and $[T_{H\to \mathrm{BL}}]$ are rotation matrices for the hub and blade reference frames. Expressions for the rotor blade reaction forces and moments are derived by taking linear acceleration of the blade and the sum of moments about the hinge point. The expressions will have inertial and aerodynamic terms; however, it is assumed that, in the hover and low-speed forward-flight regions in which the model will be used, the aerodynamic terms dominate the inertia terms. Therefore, the reaction forces and moments are approximated as

$$\begin{Bmatrix} R_X \\ R_Y \\ R_Z \end{Bmatrix} \approx -\begin{Bmatrix} F_{RA_X} \\ F_{RA_Y} \\ F_{RA_Z} \end{Bmatrix} \quad \text{and} \quad \begin{Bmatrix} m_{R_X} \\ m_{R_Z} \end{Bmatrix} \approx \begin{Bmatrix} M_{RA_X} \\ M_{RA_Z} \end{Bmatrix} \tag{18}$$

The coaxial helicopter configuration includes the lower rotor, upper rotor, and flybar. The flybar is approximated as a teetering rigid rotor that only produces drag. The upper rotor cyclic pitch inputs are controlled by the flybar through a pitch linkage. It is assumed the flybar upper rotor pitch linkages are rigid and do not affect the motion of the flybar. The relation between flybar flap angle and upper rotor pitch input is developed from linkage geometry.

The rotors are driven by brushed dc motors that are modeled as first-order systems

$$\begin{Bmatrix} \dot{\Omega}_{\mathrm{LR}} \\ \dot{\Omega}_{\mathrm{UR}} \end{Bmatrix} = \frac{1}{\tau_M}\begin{Bmatrix} C_{\mathrm{LR}}u_{\mathrm{LR}} - \Omega_{\mathrm{LR}} \\ C_{\mathrm{UR}}u_{\mathrm{UR}} - \Omega_{\mathrm{UR}} \end{Bmatrix} \tag{19}$$

where τ_M is the motor time constant, u_{LR} and u_{UR} are the motor throttle inputs, and C_{LR} and C_{UR} are the motor coefficients. The lower rotor is controlled by cyclic inputs of a swashplate, which is driven by servomotors. The swashplate angles are also modeled as first-order responses

$$\begin{Bmatrix} \dot{\theta}_{1C} \\ \dot{\theta}_{1S} \end{Bmatrix} = \frac{1}{\tau_{\mathrm{SW}}}\begin{Bmatrix} C_{\mathrm{lon}}u_{\mathrm{lon}} - \theta_{1C} \\ C_{\mathrm{lat}}u_{\mathrm{lat}} - \theta_{1C} \end{Bmatrix} \tag{20}$$

Rotor inflow is calculated using Glauert's flow model. It is assumed that the inflow is uniform across the rotor disk and is quasi-steady compared to all other vehicle dynamics. Employing the momentum theory of air moving through the rotor disk, a transcendental equation is derived and a Newton–Rhapson iteration is employed to solve for the inflow:

$$v_i^4 + 2V\sin(\alpha)v_i^3 + V^2v_i^2 = \left(\frac{T}{2\rho A}\right)^2 \tag{21}$$

The momentum theory is not valid in axial descent when the rotor wake convects back up into the rotor. Leishman [20] proposed a continuous approximation for induced inflow given by

$$\frac{v_i}{v_h} = \kappa + k_1\left(\frac{V_c}{v_h}\right) + k_2\left(\frac{V_c}{v_h}\right)^2 + k_3\left(\frac{V_c}{v_h}\right)^3 + k_4\left(\frac{V_c}{v_h}\right)^4 \tag{22}$$

where V_c is the vertical climb velocity, v_h is the inflow velocity at hover, $\kappa = 1.0$, $k_1 = -1.125$, $k_2 = -1.372$, $k_3 = -1.718$, and $k_4 = -0.655$. Equation (22) is valid for the range $-2 \le V_c/v_h \le 0$ when the vehicle is in vertical descent. Additionally, the upper rotor wake affects the inflow of the lower rotor and, for simplicity, it is assumed the wake is fully contracted. To account for the convection of the wake in forward flight, longitudinal and lateral wake skew angles are used to determine the location of the wake relative to the lower rotor. It is assumed that the lower rotor has no effect on the upper rotor. Vertical download force on the fuselage due to the rotor wakes is modeled according to Leishman [20] as

$$F_{\mathrm{DL}} = \frac{1}{2}\rho\bar{v}^2 f_{\mathrm{DL}} \tag{23}$$

where f_{DL} is the equivalent vertical flat-plate drag area, and $\bar{v}$ is the average velocity of the rotor wake.

Besides rotor forces and moments, the other external forces and moments acting on the helicopter airframe are gravity and aerodynamic drag on the fuselage and tail. The gravity forces in the body frame are

$$\begin{Bmatrix} X_G \\ Y_G \\ Z_G \end{Bmatrix} = mg\begin{Bmatrix} s_\theta \\ -s_\phi c_\theta \\ -c_\phi c_\theta \end{Bmatrix} \tag{24}$$

whereas the fuselage aerodynamic forces are modeled as a drag force acting on the vehicle center of pressure as

$$\begin{Bmatrix} X_{BA} \\ Y_{BA} \\ Z_{BA} \end{Bmatrix} = -\frac{1}{2}\rho V_{\mathrm{CP}} S\begin{Bmatrix} C_{D_x}u_{\mathrm{CP}} \\ C_{D_y}v_{\mathrm{CP}} \\ C_{D_z}w_{\mathrm{CP}} \end{Bmatrix} \tag{25}$$

where

$$V_{\mathrm{CP}} = \sqrt{u_{\mathrm{CP}}^2 + v_{\mathrm{CP}}^2 + w_{\mathrm{CP}}^2} \tag{26}$$

The aerodynamic velocity components at the center of pressure can be expressed in the body frame as

$$\begin{Bmatrix} u_{\mathrm{CP}} \\ v_{\mathrm{CP}} \\ w_{\mathrm{CP}} \end{Bmatrix} = \begin{Bmatrix} u \\ v \\ w \end{Bmatrix} + \begin{bmatrix} 0 & -r & q \\ r & 0 & -p \\ -q & p & 0 \end{bmatrix}\begin{Bmatrix} r_{\mathrm{CG}\to\mathrm{CP}_x} \\ r_{\mathrm{CG}\to\mathrm{CP}_y} \\ r_{\mathrm{CG}\to\mathrm{CP}_z} \end{Bmatrix} - \begin{Bmatrix} u_w \\ v_w \\ w_w \end{Bmatrix} \tag{27}$$

where $r_{\mathrm{CG}\to\mathrm{CP}_x}$, $r_{\mathrm{CG}\to\mathrm{CP}_y}$, and $r_{\mathrm{CG}\to\mathrm{CP}_z}$ are the position vector components from the center of mass to the center of pressure in the body frame; and u_w, v_w, and w_w are the wind components at the vehicle center of gravity that vary with time and spatial location. The body aerodynamic moments about the center of mass are

$$\begin{Bmatrix} L_{BA} \\ M_{BA} \\ N_{BA} \end{Bmatrix} = \frac{1}{2}\rho V_{\mathrm{CP}} SD^2\begin{Bmatrix} C_{l_p}p \\ C_{m_q}q \\ C_{n_r}r \end{Bmatrix} + \begin{bmatrix} 0 & -r_{\mathrm{CG}\to Cz} & r_{\mathrm{CG}\to\mathrm{CP}_y} \\ r_{\mathrm{CG}\to Cz} & 0 & -r_{\mathrm{CG}\to\mathrm{CP}_x} \\ -r_{\mathrm{CG}\to\mathrm{CP}_y} & r_{\mathrm{CG}\to\mathrm{CP}_x} & 0 \end{bmatrix}\begin{Bmatrix} X_{BA} \\ Y_{BA} \\ Z_{BA} \end{Bmatrix} \tag{28}$$

During system identification experiments, it was found that the lift forces of the vertical tail are extremely small, especially in the hover and low-speed flight regimes in which the microcoaxial helicopter operates. Thus, the lift forces are neglected and the forces and moments generated by the vertical tail are modeled as a drag force acting on the tail center of pressure.

The model parameters are fit through system identification of the commercial microcoaxial helicopter; Fig. 1. The system identification procedure involves four steps: direct measurement, estimation from benchtop experiments, flight experiments, and fine tuning. Parameters that can be directly measured through simple means (ruler, scale, etc.) include vehicle mass, rotor radius and chord, blade mass, blade collective pitch and twist, flybar mass, flybar and swashplate phase angles, upper rotor–flybar linkage lengths, motor coefficients, and distances from the reference point to the rotor hubs.

Simple benchtop tests are performed to estimate parameters that cannot be directly measured. The goal of these tests is to reduce the number of parameters that must be identified from flight experiments. The parameters identified from benchtop tests include the rotor blade effective hinge offset and spring constant, as well as the rotor blade lift and drag coefficients. The effective hinge offset and spring constant are estimated by adding weights to the blade tip and measuring the deflection. The blade cross section is a circular arc airfoil for almost the entire length. Based on this shape, the blade sectional lift and drag coefficients are estimated from airfoil theory and experimental trends

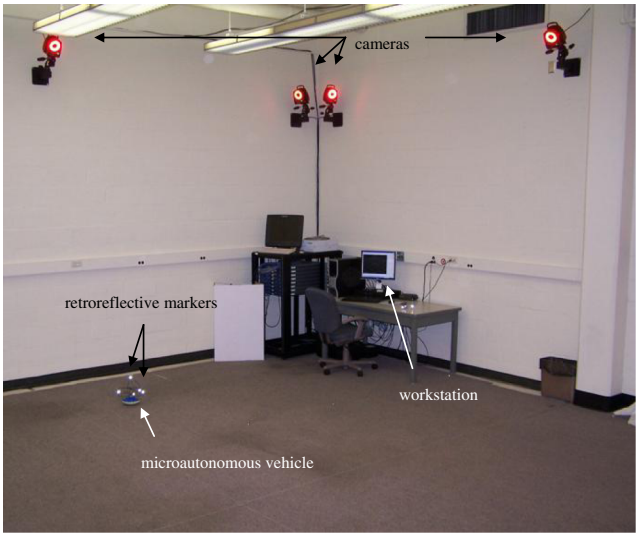

Fig. 3 Georgia Institute of Technology Indoor Flight Facility with Vicon motion-capture system.

based on the work of Katz and Plotkin [21], Prouty [22], Hoerner [23], and Costello and Beyer [24].

Piloted flight tests are performed to estimate parameters that could not be directly measured or estimated from benchtop tests. A motion-capture facility in the Georgia Institute of Technology Indoor Flight Facility (Fig. 3) using Vicon cameras measured vehicle position and attitude during flight, whereas the onboard electronics recorded control inputs and body angular rates. Flight-test maneuvers were designed to excite the steady-state and dynamic responses of the platform for each control channel, which included hover as well as vertical, yaw, roll, and pitch channel maneuvers.

An output error method is employed to estimate model parameters from a time-domain evaluation of vehicle response [25]. For each channel's maneuver, the appropriate variables are tuned to fit the channel state time histories as exemplified by the vertical channel identification data shown in Fig. 4. After flight experiments, a few final parameters including center-of-gravity location, flybar drag coefficient, and blade lift and drag coefficients are fine tuned to ensure the vehicle trims properly in hover. Additionally, the fuselage drag coefficients are tuned so that the predicted maximum flight speed matches the experimental vehicle. To validate the model, additional flight maneuvers are performed and the response simulated using the identified parameters.

Bounds for all parameters are estimated for confidence intervals of 95%. For direct measurement parameters, measurements are repeated to calculate confidence intervals using Student's t-distribution method [26]. For all other parameters, confidence intervals are estimated by inverting the "extra sum of squares" [27]. Given the vector of estimated model parameters, one parameter is fixed at a perturbed value. Then, the system identification routine is performed again and remaining model parameters are optimized. Next, a test statistic is calculated from the residual sum of squares for the perturbed model and the original model. Using the test statistic, a signed square root can be found. The signed square root is an approximation of the t statistic with a distribution of $t_{n_m-n_p}$, where n_p is the number of model parameters and n_m is the total number of measurements. Therefore, each parameter is fixed at a series of values above and below the estimated value, and the t statistic for 95% confidence and the associated parameter bounds can be found through interpolation. Table 1 shows the estimates and bounds with 95% confidence for the major model parameters.

Overall, the identified rotorcraft dynamics model captures measured motion of the experimental platform, including all major vehicle effects. The limits of the model result from some base assumptions: specifically, steady-state aerodynamics, rotor blade lift and drag profiles, and inflow approximations in the vortex ring and turbulent wake states. All these represent reasonable approximations, and the model simulates a realistic response over most of the vehicle flight envelope.

III. Extended State Observer

Consider a dynamic system of the form

$$\begin{Bmatrix} \dot{x}_1 \\ \dot{x}_2 \end{Bmatrix} = \begin{Bmatrix} x_2 \\ \tilde{F} + \tilde{G} + \Delta \end{Bmatrix} \tag{29}$$

where $\tilde{F} = \tilde{F}(x)$, $\tilde{G} = \tilde{G}(x, u)$, and Δ is the uncertainty caused by any source, such as model error and unknown external disturbances. An observer is proposed with an extended state:

$$\begin{Bmatrix} \dot{\tilde{x}}_1 \\ \dot{\tilde{x}}_2 \\ \dot{\tilde{x}}_3 \end{Bmatrix} = \begin{Bmatrix} \tilde{x}_2 + \epsilon \ell_1 \\ \tilde{F} + \tilde{G} + \tilde{x}_3 + \ell_2 \\ (1/\epsilon)\ell_3 \end{Bmatrix} \tag{30}$$

The purpose of the extended state $\tilde{x}_3$ is to estimate unknown disturbances and uncertainties. The ESO functions ℓ_1, ℓ_2, and ℓ_3 are included to guide the dynamics of the estimation error, which can be defined as $\bar{\boldsymbol{\eta}}$ where $\bar{\boldsymbol{\eta}}^T = [\eta_1 \quad \eta_2 \quad \eta_3]$ with $\eta_1 = \frac{x_1 - \tilde{x}_1}{\epsilon^2}$, $\eta_2 = \frac{x_2 - \tilde{x}_2}{\epsilon}$, and $\eta_3 = \Delta - \tilde{x}_3$. Then, the error dynamics can be expressed as

$$\dot{\eta}_1 = \frac{\dot{x}_1 - \dot{\tilde{x}}_1}{\epsilon^2} = \frac{x_2 - \tilde{x}_2 - \epsilon \ell_1}{\epsilon^2} = \frac{\eta_2 - \ell_1}{\epsilon} \tag{31}$$

$$\dot{\eta}_2 = \frac{\dot{x}_2 - \dot{\tilde{x}}_2}{\epsilon} = \frac{\Delta - \tilde{x}_3 - \ell_2}{\epsilon} = \frac{\eta_3 - \ell_2}{\epsilon} \tag{32}$$

$$\dot{\eta}_3 = \dot{\Delta} - \frac{\ell_3}{\epsilon} = \frac{\epsilon \dot{\Delta} - \ell_3}{\epsilon} \tag{33}$$

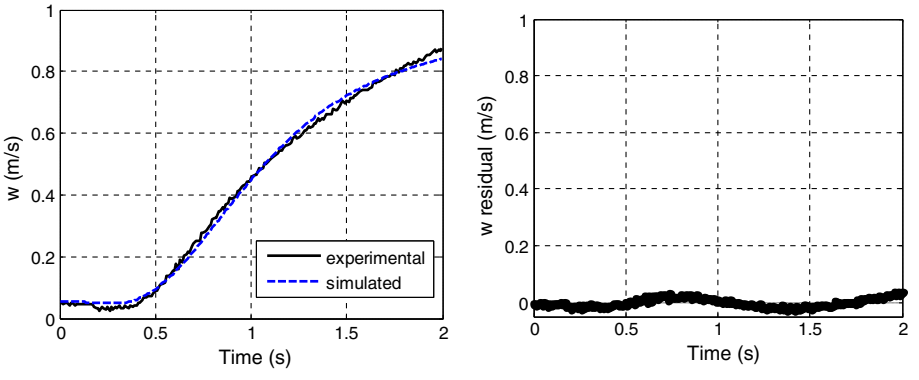

a) b)

Fig. 4 Vertical channel identification: a) w velocity fit, and b) w velocity residual.

Table 1 Helicopter model parameter confidence intervals

Parameter	Description	Mean value	Lower bound	Upper bound	Units	Source of bounds
m	Vehicle mass	0.06038	0.06037	0.06039	kg	Measured
I_{xx}	Vehicle mass moment of inertia: x	4.952E − 5	3.878E − 5	6.570E − 5	kg · m^2	Inverting sum of squares
I_{yy}	Vehicle mass moment of inertia: y	1.603E − 4	1.347E − 4	2.060E − 4	kg · m^2	Inverting sum of squares
I_{zz}	Vehicle mass moment of inertia: z	1.028E − 6	5.138E − 7	1.541E − 6	kg · m^2	Inverting sum of squares
C_{dx}	Vehicle drag coefficient: x	0.5501	0.4859	0.6143	nd	Inverting sum of squares
C_{dy}	Vehicle drag coefficient: y	0.2979	0.2532	0.3426	nd	Inverting sum of squares
C_{dz}	Vehicle drag coefficient: z	7.880	7.670	8.091	nd	Inverting sum of squares
τ_{SW}	Swashplate servomotor time constant	0.0999	0.0499	0.1499	s	Inverting sum of squares
C_{l_p}	Roll damping coefficient	−9.595	−13.400	−5.790	nd	Inverting sum of squares
C_{m_q}	Pitch damping coefficient	−10.325	−14.130	−6.520	nd	Inverting sum of squares
C_{n_r}	Yaw damping coefficient	−6.234	−6.764	−5.659	nd	Inverting sum of squares
m_b	Blade mass	9.6E − 4	9.031E − 4	1.017E − 3	kg	Measured
I_{bxx}	Blade mass moment of inertia: x	1.4E − 8	1.3E − 8	1.5E − 8	kg · m^2	Inverting sum of squares
I_{byy}	Blade mass moment of inertia: y	6.3E − 7	5.3E − 7	7.3E − 7	kg · m^2	Inverting sum of squares
I_{bzz}	Blade mass moment of inertia: z	6.44E − 7	6.43E − 7	6.45E − 7	kg · m^2	Inverting sum of squares
R	Rotor radius	8.858E − 2	8.824E − 2	8.892E − 2	m	Measured
e	Nondimensional blade hinge offset	0.218	0.196	0.24	nd	Inverting sum of squares
k_β	Blade effect hinge spring constant	0.095	0.08	0.11	N · m/rad	Inverting sum of squares
τ_M	Motor time constant	0.100	0.083	0.117	s	Inverting sum of squares
$\mathrm{m_{FB}}$	Flybar mass	0.001	9.9990E − 04	1.0010E − 03	kg	Inverting sum of squares
θ_{twist}	Blade pitch twist	−0.2614	−0.2963	−0.2265	rad	Measured
θ_0	Blade collective pitch	0.3749	0.3400	0.4098	rad	Measured

nd, nondimensional.

or in vector form as

$$\dot{\bar{\boldsymbol{\eta}}} = \begin{Bmatrix} \dot{\eta}_1 \\ \dot{\eta}_2 \\ \dot{\eta}_3 \end{Bmatrix} = \frac{1}{\epsilon} \begin{Bmatrix} \eta_2 - \ell_1 \\ \eta_3 - \ell_2 \\ \epsilon\dot{\Delta} - \ell_3 \end{Bmatrix} \tag{34}$$

The objective is to design the observer such that $\bar{\boldsymbol{\eta}}$ is driven to a small value with stable error dynamics. The stability of the error dynamics can be examined through Lyapunov stability theory. Given the Lyapunov function

$$V = \frac{1}{2}\bar{\boldsymbol{\eta}}^T\bar{\boldsymbol{\eta}} \tag{35}$$

the time derivative of the function is

$$\dot{V} = \frac{1}{2}(\dot{\bar{\boldsymbol{\eta}}}^T\bar{\boldsymbol{\eta}} + \bar{\boldsymbol{\eta}}^T\dot{\bar{\boldsymbol{\eta}}}) = \bar{\boldsymbol{\eta}}^T\dot{\bar{\boldsymbol{\eta}}} \tag{36}$$

Substituting in Eq. (34) and removing the constant $1/\epsilon$ without the loss of generality, Eq. (36) becomes

$$\dot{V} = \eta_1(\eta_2 - \ell_1) + \eta_2(\eta_3 - \ell_2) + \eta_3(\epsilon\dot{\Delta} - \ell_3) \tag{37}$$

which can be rearranged as

$$\dot{V} = [\eta_1(\eta_2 - \ell_1) - \eta_2\ell_2] + \eta_3(\eta_2 + \epsilon\dot{\Delta} - \ell_3) \tag{38}$$

Thus, the ESO functions can be designed as

$$\ell_1 = \eta_2 + k_1\,\mathrm{sat}(\eta_1, \delta_1) \tag{39}$$

$$\ell_2 = k_2\,\mathrm{sat}(\eta_2, \delta_2) \tag{40}$$

$$\ell_3 = k_3\eta_2 \tag{41}$$

where $\mathrm{sat}(\eta, \delta)$ is a saturation function with a boundary layer:

$$\mathrm{sat}(\eta, \delta) = \begin{cases} \eta/\delta & \text{if } |\eta/\delta| \le 1 \\ \mathrm{sign}(\eta) & \text{if } |\eta/\delta| > 1 \end{cases} \tag{42}$$

Equation (38) can then be rewritten as

$$\dot{V} = [-k_1\eta_1\,\mathrm{sat}(\eta_1, \delta_1) - k_2\eta_2\,\mathrm{sat}(\eta_2, \delta_2)] + \eta_3(\epsilon\dot{\Delta} - \eta_2(k_3 - 1)) \tag{43}$$

It is reasonable to assume that the uncertainty and external disturbances are bounded; thus, $\eta_3 \le \mathbb{M}$ and $|\dot{\Delta}| \le \mathbb{N}$:

$$\dot{V} \le [-k_1\eta_1\,\mathrm{sat}(\eta_1, \delta_1) - k_2\eta_2\,\mathrm{sat}(\eta_2, \delta_2)] - \eta_2\mathbb{M}(k_3 - 1) + \eta_3\epsilon\mathbb{N} \tag{44}$$

Therefore ϵ, k_1, k_2, and k_3 can be selected so $\dot{V} \le 0$, and the error dynamics are bounded and stable. Methods of estimating $\mathbb{N}$ in Eq. (44) are dependent on the type of system. For systems where the user is confident of the accuracy of the model, the simulation model can be leveraged. Errors added to model parameters and external disturbances can be propagated through the simulation to calculate the uncertainty and its corresponding derivative. By looking at the expected errors and disturbances, the bounds of the uncertainty parameters can be estimated. This can be performed analytically for simpler models or numerically for complex nonlinear models. For systems with unmodeled or highly unknown dynamics, an experimental approach can be taken. Experimental measurements can be postprocessed using the ESO model to calculate the uncertainty. By measuring the system under various conditions, the bounds can be estimated.

IV. Mass Properties Estimation Algorithm with ESO

Extended state observers provide a bounded converging estimation of the total disturbances acting on a dynamic system. The disturbances due to mass and center-of-gravity model errors can be isolated and used to improve parameter estimates. Filters are designed to use the observer states as feedback to update mass and CG parameter estimates

$$\begin{Bmatrix} \dot{m} \\ \dot{\tilde{r}}_{\mathrm{CG}_x} \\ \dot{\tilde{r}}_{\mathrm{CG}_y} \\ \dot{\tilde{r}}_{\mathrm{CG}_z} \end{Bmatrix} = \begin{Bmatrix} f_m(\tilde{x}, \dot{\tilde{x}}) \\ f_{\mathrm{CG}_x}(\tilde{x}, \dot{\tilde{x}}) \\ f_{\mathrm{CG}_y}(\tilde{x}, \dot{\tilde{x}}) \\ f_{\mathrm{CG}_z}(\tilde{x}, \dot{\tilde{x}}) \end{Bmatrix} \tag{45}$$

where $\tilde{x} = [\,\tilde{x}_1 \quad \tilde{x}_2 \quad \tilde{x}_3\,]^T$. There are many possible filter designs to isolate the uncertainties to estimate mass properties. As seen in Fig. 5, model errors in mass, longitudinal CG location, and lateral CG

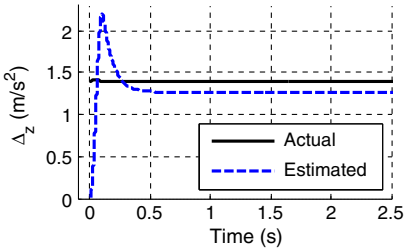

Fig. 5 Uncertainty in z state due to mass error, actual and estimated, from the ESO during hover.

location primarily produce constant or low-frequency disturbances in the z, pitch, and roll states, respectively, which affect the trim states for the helicopter. Thus, simple filters are employed to estimate mass and horizontal CG location as functions of the z, roll, and pitch disturbance states. The filters, as shown in Eq. (46), isolate the low-frequency content of the estimated uncertainty states:

$$\begin{aligned} f_m &= k_{p_m}\tilde{x}_{3_z} + k_{d_m}\dot{\tilde{x}}_{3_z} \\ f_{\mathrm{CG}_x} &= k_{p_{\mathrm{CG}_x}}\tilde{x}_{3_\theta} + k_{d_{\mathrm{CG}_x}}\dot{\tilde{x}}_{3_\theta} \\ f_{\mathrm{CG}_y} &= k_{p_{\mathrm{CG}_y}}\tilde{x}_{3_\phi} + k_{d_{\mathrm{CG}_y}}\dot{\tilde{x}}_{3_\phi} \end{aligned} \tag{46}$$

The vertical CG location is almost always dominated by other uncertainties, but test simulations identified a pattern that is clearer during roll and pitch maneuvers after horizontal CG location estimates have settled out. Using this pattern, the filter used for vertical CG estimation is

$$f_{\mathrm{CG}_z} = k_{z1} f_{\mathrm{DB}}(\dot{\tilde{x}}_{3_\phi}, \alpha_\phi)\dot{\tilde{\phi}} + k_{z2} f_{\mathrm{DB}}(\dot{\tilde{x}}_{3_\theta}, \alpha_\theta)\dot{\tilde{\theta}} \tag{47}$$

where f_{DB} is a deadband function:

$$f_{\mathrm{DB}}(x, \alpha) = \begin{cases} x, & |x| \le \alpha \\ 0, & |x| > \alpha \end{cases} \tag{48}$$

Figure 6 shows example time-history estimations of vehicle mass and CG location for a helicopter in hover with a discrete change in mass properties after 1 s. The discrete change is meant to simulate a rotorcraft performing a payload dropoff. Mass, longitudinal CG, and lateral CG estimates all converge quickly, within 3 to 5 s. With very little excitation during hover, the vertical CG estimate converges slowly to within 1 mm accuracy.

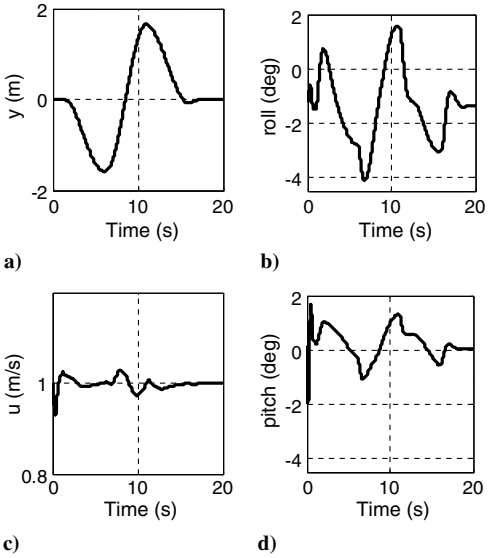

Fig. 7 Low-speed forward-flight maneuver: a) y position, b) roll attitude, c) body forward-flight velocity, and d) pitch attitude.

To make vertical CG more observable, a roll maneuver during forward flight is simulated, as seen in Fig. 7, with Fig. 8 showing time-history examples of the mass property estimates. Estimation of the vertical CG is improved, whereas all other mass property estimates remain accurate. Figure 8d shows good estimation; however, it is clear that vertical CG position is difficult to isolate, particularly with model mismatch and measurement noise.

Although changing model parameters in flight does feed back into the ESO, as long as the time derivative of the uncertainty ($\dot{\Delta}$) remains within prescribed bounds $\mathbb{N}$, the observer remains stable. This can be ensured by setting the mass and CG estimation filter gains in Eqs. (46) and (47) so the parameter estimates change slowly. For this system, the majority of the uncertainty is due to mass and CG errors, which results in constant uncertainty. Thus, the filter gains can be tuned similar to a PD control loop for a step response.

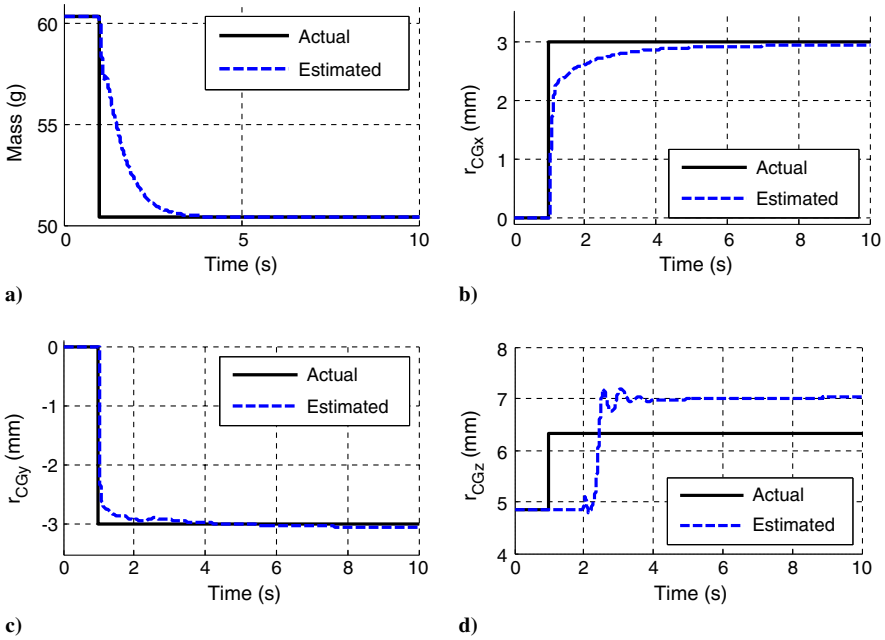

Fig. 6 Estimation of mass properties during a payload dropoff in hover: a) mass, b) longitudinal center-of-gravity position, c) lateral center-of-gravity position, and d) vertical center-of-gravity position.

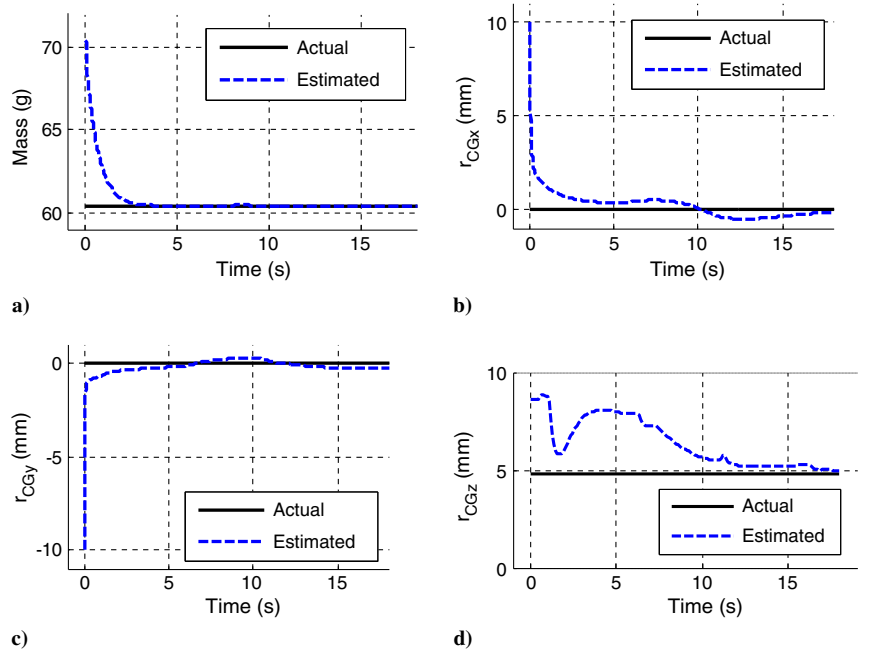

Fig. 8 Estimation of mass properties during forward-flight maneuver: a) mass, b) longitudinal center-of-gravity position, c) lateral center-of-gravity position, and d) vertical center-of-gravity position.

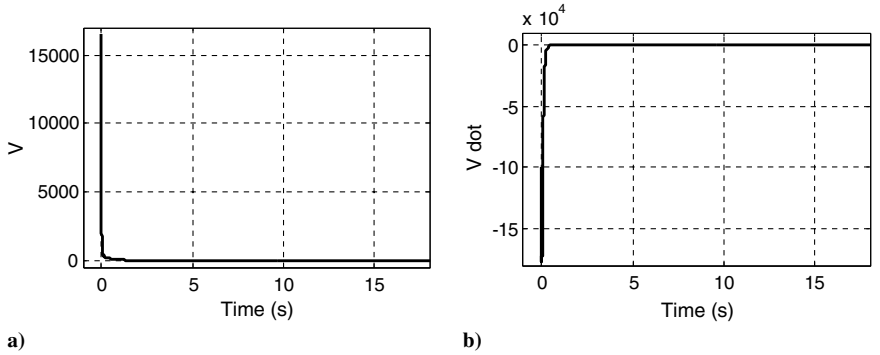

Fig. 9 Example time history of a candidate Lyapunov function for an extended state observer with mass property estimation: a) Lyapunov function, and b) Lyapunov function time derivative.

Thus, the helicopter model uncertainty due to mass and CG errors can be driven to zero as part of the observer design process. Figure 9 shows the Lyapunov function from Eq. (35) and the time derivative from Eq. (36) for the example forward-flight maneuver. After starting with large initial errors, the Lyapunov function is driven to zero with a negative time derivative.

V. Monte Carlo Simulations

To assess the accuracy, robustness, and behavior of the mass and CG estimation algorithm presented, Monte Carlo simulations are performed with the nonlinear rotorcraft flight dynamics model developed in Sec. II. Simulations use the forward-flight maneuver described in Sec. IV while varying model and measurement errors to capture realistic performance of the algorithm. The confidence intervals calculated during model validation (Table 1) are used to derive mean and standard derivations for Gaussian distributions of each model parameter to add model mismatch to the ESO. Simulations are performed for 250 cases; and for each case, model parameters are initialized based on these distributions.

State measurements for the Monte Carlo simulations include the measurement error from sensor noise and bias. Errors are modeled as exponentially correlated Gaussian noise with the measurement signals taking the form

$$\begin{aligned} v_k &= y_k + n_k \\ n_k &= e^{-\Delta t/\tau} n_{k-1} + \xi_k \sqrt{1 - e^{-2\Delta t/\tau}} \\ \xi_k &\sim N(0, \sigma_N) \end{aligned} \tag{49}$$

where y_k is the actual value, v_k is the measurement value, n_k is the measurement noise, and Δt is the time between measurements. The measurement error parameters (σ_N, τ) are tuned based on realistic sensor signals from a Vicon motion-capture system for position, attitude, and linear velocity and from low-cost microelectromechanical system rate gyroscopes for angular velocity. Measurement error parameter values for the trade study simulations are shown in Table 2. It should be noted that, although the sensor signal errors simulated here are based on a Vicon system, the only requirement for the ESO framework is to provide full-state feedback. This can be achieved through fusion of available sensors, such as GPS, IMU, altimeter, and magnetometer.

Figure 10 shows histograms of the mass property estimations for Monte Carlo simulations with baseline model error and measurement noise. Mean estimates for vehicle mass, longitudinal CG position, and lateral CG position are all accurate with small standard deviations, as can also be seen in Table 3. Vertical CG estimates are poor with a large mean error and standard deviation. As expected, the cause of poor vertical CG estimation is the much smaller uncertainty

Table 2 Measurement error parameters

Signal	σ_N	Units	τ, s
x	1.01E − 04	m	0.01
y	6.2E − 05	m	0.01
z	5.6E − 05	m	0.01
φ	0.02634	deg	0.01
θ	0.02434	deg	0.01
ψ	0.04126	deg	0.01
u	0.01	m/s	0.01
v	0.01	m/s	0.01
w	0.01	m/s	0.01
p	5.0	deg /s	0.001
q	5.0	deg /s	0.001
r	2.5	deg /s	0.001

Table 3 Trade study mean and standard deviations of estimated mass properties with baseline model error and measurement noise

Parameter	Mean	Standard deviation	Actual value
Vehicle mass, g	59.90	2.33	60.38
r_{CG_x}, mm	−0.27	1.23	0.00
r_{CG_y}, mm	−0.11	1.22	0.00
r_{CG_z}, mm	9.74	5.44	4.83

due to vertical CG mismatch being dominated by other sources of uncertainty.

Although the 0.5 g accuracy of the mass estimation is excellent and straightforward to understand, the millimeter accuracy of the longitudinal and lateral CG estimates are difficult to place in context. Pilot observations during experimental flight testing with the commercial microhelicopter estimated the horizontal variation in the platform CG to be approximately 12 mm. Given this possible range, 1 mm errors in horizontal CGs are accurate estimations representing 1.4% of the rotor radius, whereas the possible CG range is 13%. Projecting the algorithm's accuracy to manned helicopters, Table 4 shows reported longitudinal CG ranges for the UH-1, AH-64, and UH-60 helicopters [28–30]. Even though the larger rotorcraft have considerably less CG travel than the microcoaxial helicopter, assuming similar algorithm performance, the ESO framework would perform adequately for the UH-1 and UH-60. However, the very small range of the AH-64 would be difficult. The known CG bounds could also be incorporated in the filters, which may improve estimation accuracy.

In addition to Monte Carlo simulations with a baseline model error, two other scenarios were executed to assess the effect of model error on algorithm performance. Given the baseline confidence intervals, analogs with a half-model error and double-model error were considered by scaling the bounds for all parameters appropriately. Table 5 shows the helicopter mass property estimate means and standard deviations for half-, baseline-, and double-model errors. As expected, accuracy decreases for increasing model error, which can particularly be seen by the large increases in estimate standard deviations.

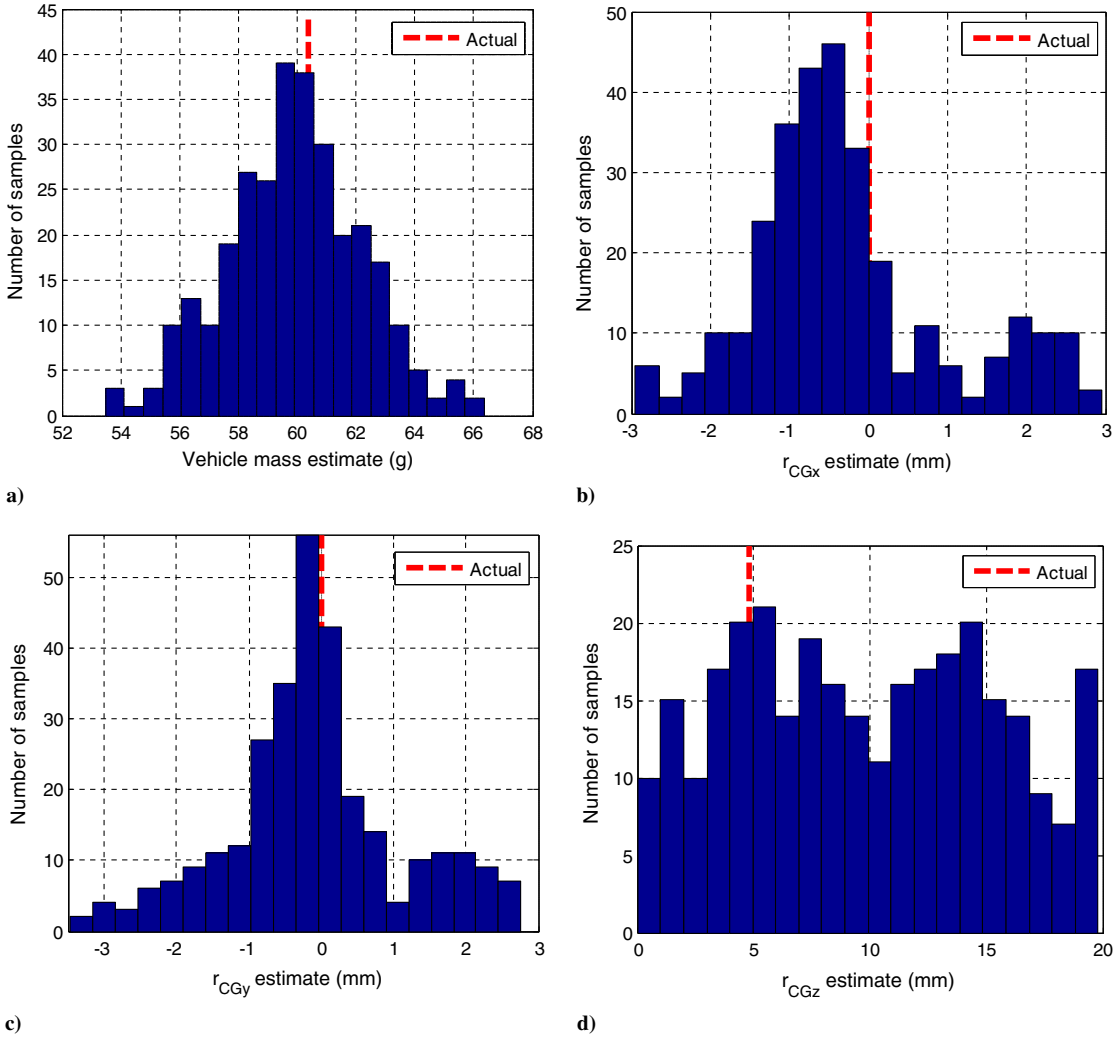

Fig. 10 Histograms of helicopter mass property estimation: a) mass, b) longitudinal center-of-gravity position, c) lateral center-of-gravity position, and d) vertical center-of-gravity position.

Table 4 Expected longitudinal center-of-gravity ranges for manned and unmanned helicopters

	CG range	Rotor radius	CG range as percentage of rotor radius
Microcoaxial helicopter	12 mm	88 mm	13.64
Bell UH-1 Iroquois [28]	14 in.	24 ft	4.86
Boeing AH-64 Apache [29]	6 in.	24 ft	2.08
Sikorsky UH-60 Black Hawk [30]	23 in.	26.83 ft	7.14

Table 5 Trade study mean and standard deviations for mass properties

Parameter	Model error	Mean	Standard deviation	Actual value
Vehicle mass estimate, g	Half	59.98	1.33	60.38
	Baseline	59.90	2.33	
	Double	59.76	4.06	
r_{CG_x} estimate, mm	Half	−0.32	1.14	0.00
	Baseline	−0.27	1.23	
	Double	−0.26	1.33	
r_{CG_y} estimate, mm	Half	−0.06	1.08	0.00
	Baseline	−0.11	1.22	
	Double	−0.26	1.33	
r_{CG_z} estimate, mm	Half	9.60	5.41	4.83
	Baseline	9.74	5.44	
	Double	10.29	5.78	

VI. Conclusions

A new method for real-time estimation of helicopter mass properties based on an extended state observer framework has been developed. An important feature of the algorithm is the ability to be proven stable even for nonlinear systems. The extended state observermethod was applied to the estimation of vehicle mass and center-of-gravity position for a validated nonlinear dynamic model of a 60 g commercial radio-controlled coaxial helicopter. To assess the performance of the mass estimation algorithm for this simulation model, Monte Carlo trade studies were performed. Trade study cases included measurement noise and varying model parameter errors, but unmodeled dynamics were neglected. Trade study results demonstrated the effectiveness of the new method for estimating vehicle mass, longitudinal center of gravity, and lateral center of gravity in the presence of expected measurement and model errors. Estimation of the vertical center-of-gravity (CG) position was poorer due to the limited observability of errors due to vertical CG mismatch. The many benefits from inflight estimation of helicopter mass and center of gravity (such as improved maintenance systems and reduced operating costs, enhanced safety and reliability, and better control system gain scheduling and trajectory generation) are well known. Since rotorcraft often operate in nonlinear flight regimes, normal missions may require a nonlinear parameter estimation algorithm such as the ESO method presented here to reliably estimate mass properties.

References

[1] Bateman, C., "Weight, Balance, and Tire Pressure Detection Systems," U.S. Patent 4312042 A, Jan. 1982.

[2] Glover, J., "Aircraft In-Flight Center of Gravity Measuring System," U.S. Patent 4545019 A, Oct. 1985.

[3] Moffatt, J., "Helicopter Gross Weight Determination from Monitored," U.S. Army Aviation and Troop Command TR-96-D-5, Fort Eustis, VA, 1986.

[4] Morales, M., and Haas, D., "Feasiblity of Aircraft Gross Weight Estimation Using Artificial Neural Networks," *American Helicopter Society 57th Annual Forum*, AHS International, Fairfax, VA, 2001, pp. 1872–1880.

[5] Bi, N. B., Haas, D. J., and McCool, K., "Investigation of the In-Flight Gross Weight and CG Estimation of the V-22 Aircraft," *American Helicopter Society 60th Annual Forum*, AHS International, Fairfax, VA, June 2004.

[6] Idan, M., Iosilevskii, G., and Nazarov, S., "In-Flight Weight and Balance Identification Using Neural Networks," *Journal of Aircraft*, Vol. 41, No. 1, 2004, pp. 137–143. doi:10.2514/1.592

[7] Abraham, M., and Costello, M., "In-Flight Estimation of Helicopter Gross Weight and Mass Center Location," *Journal of Aircraft*, Vol. 46, No. 3, 2009, pp. 1042–1049. doi:10.2514/1.41018

[8] Taylor, B., and Rogers, J., "Experimental Investigation of Real-Time Helicopter Weight Estimation," *Journal of Aircraft*, Vol. 51, No. 3, May–June 2014, pp. 1047–1051. doi:10.2514/1.C032449

[9] Apetre, N., Sarkar, S., Iyyer, N., and Phan, N., "Innovative Methods to Estimate Rotorcraft Gross Weight and Center of Gravity," *American Helicopter Society 67th Annual Fourm*, AHS International, Fairfax, VA, 2011.

[10] Simon, D., *Optimal State Estimation: Kalman, H Inifinity, and Nonlinear Approaches*, Wiley-Interscience, Hoboken, NJ, 2006, pp. 123–139, 336–337, 395–410.

[11] Han, J. Q., "A Class of Extended State Observers for Uncertain Systems," *Control and Decision*, Vol. 10, No. 1, 1995, pp. 85–88 (in Chinese).

[12] Han, J., "From PID to Active Disturbance Rejection Control," *IEEE Transactions on Industrial Electrionics*, Vol. 56, No. 3, 2009, pp. 900–906. doi:10.1109/TIE.2008.2011621

[13] Hou, Y., Gao, Z., Jiang, F., and Bolter, B., "Active Disturbance Rejection Control for Web Tension Regulation," *Proceedings of the 40th IEEE Conference on Decision and Control*, Vol. 5, IEEE Publ., Piscataway, NJ, 2001. doi:10.1109/.2001.980997

[14] Su, Y., Duan, B. Y., Zheng, C. H., Zhang, Y. F., Chen, G. D., and Mi, J. W., "Disturbance-Rejection High-Precision Motion Control of a Stewart Platform," *IEEE Transactions on Control Systems Technology*, Vol. 12, No. 3, 2004, pp. 364–374. doi:10.1109/TCST.2004.824315

[15] Huang, Y., Kekang, X., Jingqing, H., and Lam, J., "Flight Control Design Using Extended State Observer and Non-Smooth Feedback," *Proceedings of the 40th IEEE Conference on Decision and Control*, Vol. 1, IEEE Publ., Piscataway, NJ, 2001. doi:10.1109/.2001.980102

[16] Martini, A., Léonard, F., and Abba, G., "Dynamic Modelling and Stability Analysis of Model-Scale Helicopters Under Wind Gust," *Journal of Intelligent and Robotic Systems*, Vol. 54, No. 4, 2009, pp. 647–686. doi:10.1007/s10846-008-9280-z

[17] Léonard, F., Martini, A., and Abba, G., "Robust Nonlinear Controls of Model-Scale Helicopters Under Lateral and Vertical Wind Gusts," *IEEE Transactions on Control Systems Technology*, Vol. 20, No. 1, 2012, pp. 154–163. doi:10.1109/TCST.2010.2102023

[18] Mehta, A., and Pister, K., "WARPWING: A Complete Open Source Control Platform for Miniature Robots," *2010 IEEE/RSJ International Conference on Intelligent Robots and Systems (IROS 2010)*, IEEE Publ., Piscataway, NJ, 2010.

[19] Johnson, W., *Helicopter Theory*, Princeton Univ. Press, Princeton, NJ, 1980, pp. 184–193.

[20] Leishman, J. G., *Principles of Helicopter Aerodynamics*, Cambridge Univ. Press, Cambridge, England, U.K., 2006, pp. 87, 388.

[21] Katz, J., and Plotkin, A., *Low-Speed Aerodynamics: From Wing Theory to Panel Methods*, McGraw–Hill, New York, 1991, pp. 156–158.

[22] Prouty, R., *Helicopter Performance, Stability, and Control*, Krieger, Malabar, FL, 2005.

[23] Hoerner, S., *Fluid-Dynamic Drag: Practical Information on Aerodynamic Drag and Hydrodynamic Resistance*, Hoerner Fluid Dynamics, Bakersfield, CA, 1985.

[24] Costello, M., and Beyer, E., "Performance of a Projectile/Rotor Kinetic Energy Reduction System," *AHS International Specialists' Meeting — Unmanned Rotorcraft: Design*, AHS International, Fairfax, VA, 2007.

[25] Klein, V., and Morelli, E., *Aircraft System Identification: Theory and Practice*, AIAA, Reston, VA, 2006, pp. 191–196.

[26] Wheeler, A. J., and Ganji, A. R., *Introduction to Engineering Experimentation*, 2nd ed., Person Prentice–Hall, Upper Saddle River, NJ, 2004, pp. 142–144.

[27] Venables, W. N., and Ripley, B. D., *Modern Applied Statistics with S*, Springer Science+Business Media, New York, 2002, pp. 220–226.
[28] Anon., "Operator's Manual: Army Model UH-1H/V Helicopters," Headquarters, U.S. Dept. of the Army Technical Manual TM-55-1520-210-10, Feb. 1988.
[29] Anon., "Operator's Manual for Helicopter, Attack, AH-64A Apache," Headquarters, U.S. Dept. of the Army Technical Manual TM-1-1520-238-10, Aug. 1994.
[30] Howlett, J. J., "UH-60A Black Hawk Engineering Simulation Program, Volume 1: Mathematical Model," NASA CR-166309, Dec. 1981.